View metadata, citation and similar papers at core.ac.uk

brought to you by CORE

provided by Elsevier - Publisher Connector

Available online at www.sciencedirect.com

ScienceDirect

International Journal of Solids and Structures 44 (2007) 8006–8027

INTERNATIONAL JOURNAL OF SOLIDS AND STRUCTURES

www.elsevier.com/locate/ijsolstr

Buckling analysis of laminated composite plates containing delaminations using the enhanced assumed strain solid element

Sang-Youl Lee [a,*], Dae-Yong Park [b]

[a] *Department of Civil Engineering, Hanyang University, 17 Haedang-dong Sungdong-Gu, Seoul 133-791, Republic of Korea*
[b] *Bridge Engineering Team, Daelim Industrial Co. Ltd., Susong-Dong, Jongno-Gu, Seoul 100-732, Republic of Korea*

Received 5 February 2007; received in revised form 26 May 2007
Available online 2 June 2007

Abstract

This study investigates buckling behaviors of laminated composite structures with a delamination using the enhanced assumed strain (EAS) solid element. The EAS three-dimensional finite element (FE) formulation described in this paper, in comparison with the conventional approaches, is more attractive not only because it shows better accuracy but also it converges faster, especially for distorted element shapes. The developed FE model is used for studying cross-ply or angle-ply laminates containing an embedded delamination as well as through-the-width delamination. The numerical results obtained are in good agreement with those reported by other investigators. In particular, new results reported in this paper are focused on the significant effects of the local buckling for various parameters, such as size of delamination, aspect ratio, width-to-thickness ratio, stacking sequences, and location of delamination and multiple delaminations.
© 2007 Elsevier Ltd. All rights reserved.

Keywords: EAS solid finite element; Local buckling; Laminated composite structures; Through-the-width delamination; Embedded delamination; Anisotropic material

1. Introduction

It is known that delaminations are the most frequent causes of failure in laminated structures, particularly under compressive loads. The delaminations in composite materials may occur as a result of various reasons such as manufacturing imperfections, imperfections of various natures, external impacts, thermal and chemical shrinkage of components, and high stress concentrations in the area of geometric or material discontinuities. The presence of delaminations in composite laminates can reduce the overall stiffness and cause the material unbalance in a symmetric laminate. In addition, delaminations tend to grow rapidly under postbuckling loads, causing further reductions in the structural strength and leading ultimately to the fatal structural failure.

For the past two decades, analytical and numerical analyses have been carried out by many researchers to analyze delaminated composite structures, considering their buckling and postbuckling behaviors. Chai et al.

* Corresponding author. Tel.: +82 2 2253 8330; fax: +82 24009134.
E-mail addresses: leesy72@hanyang.ac.kr, leesangyoul@hanmail.net (S.-Y. Lee).

0020-7683/$ - see front matter © 2007 Elsevier Ltd. All rights reserved.
doi:10.1016/j.ijsolstr.2007.05.023

(1981) presented an one-dimensional analytical model to assess the compressive strength of delaminated composites. Simitses et al. (1985) investigated delamination buckling and growth by using one-dimensional beam-plate theory. The problem of symmetric local buckling and growth of a delamination in a circular plate was presented by Bottega and Maewal (1983). Sheinman and Soffer (1990) extended the work of Simitses et al. (1985) to include the effect of extension-bending coupling on the stability of a delaminated composite by using a finite-difference method. Kardomateas and Schmueser (1988) studied the effects of the transverse shear on the buckling and postbuckling of delaminated composites. Chen (1991) investigated transverse shear effects by using variational energy principles. His study presented that the transverse shear effect depends on the location and length of the delamination. The buckling analysis of beam-plate having multiple delaminations has been analyzed by Suemasu et al. (1998) and Wang et al. (1997). Jane and Yin (1992) developed an analytical procedure, based on the Rayleigh–Ritz method and von Karman's nonlinear theory of plates, for computing the buckling load and the postbuckling solution of cross-ply and angle-ply sub-laminates by the thin-film approximation. Whitcomb (1989) studied the delamination growth caused by the local buckling in composite laminates that have a near-surface delamination, by using the geometrically nonlinear finite element. Buckling analysis using the FEM based on the Mindlin plate theory, which includes contact algorithms, has been performed by Hu (1999). Several investigators proposed models based on higher-order theories for more accurate prediction of buckling loads. For instance, Gu and Chattopadhyay (1999) developed a new higher-order theory to analyze the delamination buckling problem. Their results showed that the transverse shear effect is significant for delamination buckling. This theory, however, employs a lot of primary variables with increasing number of delamination.

In these works, in the conventional two-dimensional finite element model based on Reissner/Mindlin plate theory or classical plate theory, at the edge of the delamination the node of the element are rigidly connected together using offset vectors. However, the numerical implementation of these offset vectors cause additional complexity in the problem of the laminates with multiple delaminations having an arbitrary shape, location, and size. In order to overcome additional connected elements nor offset vectors to model delaminations in the damaged composites, Cheng et al. (1996) proposed a model based on a higher-order zig-zag theory for composite laminates with the weakened interface. But this model could not describe both the slipping and opening of delaminations. A finite element based on the efficient higher-order zig-zag theory with multiple delaminations was developed by Kim and Cho (2002), but it has a complicate formulation and is limited in cross-ply laminates. Furthermore, most of the papers on the delamination buckling and postbuckling behavior of composite laminates are restricted to a through-the-width or a near-surface delamination and are also restricted to cross-ply laminates. However, the embedded delamination is more important issue from the engineering point of view, which cannot be analyzed by means of one-dimensional model or thin-film approximation. A two-dimensional model based on higher-order theories is mainly employed to analyze the embedded delaminations, however, its capability to investigate the local buckling mode at the delamination face is limited. On the other hand, the solid finite element investigated in this study can illustrate the more accurate local buckling mode at the delamination zone. Moreover, computations using the EAS element are free from shear locking and can yield accurate results for distorted element shapes (Braes, 1998). This allows the convenient use of EAS elements. A variety of EAS formulations exist, but they are mostly applicable to the two-dimensional analysis of plates made of isotropic materials. In this paper, the existing solid EAS elements are further extended to study structures made of anisotropic materials. This study focuses on the interaction between the local and global buckling behaviors of laminated composite plates for various parameters, such as the delamination size, aspect ratio, width-to-thickness ratio, stacking sequences, and location of delamination and multiple delaminations.

2. Theoretical formulation

2.1. Enhanced assumed strain field

The variational basis of the finite element method with enhanced assumed strain (EAS) fields is based on the principle of Hu-Washizu in the following:

$$\prod_{\mathbf{HW}}(\mathbf{u},\boldsymbol{\varepsilon},\boldsymbol{\sigma}) = \int_V \left[\frac{1}{2}\boldsymbol{\varepsilon}^{\mathbf{T}}\mathbf{C}\boldsymbol{\varepsilon} + \boldsymbol{\sigma}^{\mathbf{T}}(\boldsymbol{\varepsilon}^{\mathbf{c}} - \boldsymbol{\varepsilon})\right] \mathrm{d}V + \prod_{\mathrm{ext}}(\mathbf{u})$$

$$\prod_{\mathrm{ext}}(\mathbf{u}) = -\int_V \mathbf{u}^{\mathbf{T}}\bar{\mathbf{b}}\,\mathrm{d}V - \int_{S_\sigma} \mathbf{u}^{\mathbf{T}}\bar{\mathbf{t}}\,\mathrm{d}S - \int_{S_u} \mathbf{t}^{\mathbf{T}}(\mathbf{u}-\bar{\mathbf{u}})\,\mathrm{d}S \tag{1}$$

where displacement field $\mathbf{u}$, strains $\boldsymbol{\varepsilon}$, and stresses $\boldsymbol{\sigma}$ are the free variables, $\mathbf{C}$ stands for the material stiffness matrix. Prescribed values are marked by an upper bar, namely body force $\bar{\mathbf{b}}$, surface traction $\bar{\mathbf{t}}$, and the boundary conditions $\bar{\mathbf{u}}$ for prescribed displacements.

Following the idea of Simo and Rifai (1990), the assumed strains in the finite element calculations can be now split into a *compatible* part $\boldsymbol{\varepsilon}^{\mathbf{c}}$ that satisfies the geometric field equations in the strong sense and an *enhanced* part $\tilde{\boldsymbol{\varepsilon}}$

$$\boldsymbol{\varepsilon} = \boldsymbol{\varepsilon}^{\mathbf{c}} + \tilde{\boldsymbol{\varepsilon}} = \mathbf{B}\mathbf{u} + \mathbf{M}\boldsymbol{\alpha} \tag{2}$$

where $\mathbf{B}$ is the compatible strain–displacement relation matrix, $\mathbf{M}$ is the interpolation matrix for the enhanced assumed strain fields, and $\boldsymbol{\alpha}$ is the vector of the internal strain parameters corresponding to the enhanced strain.

By substituting Eq. (2) into Eq. (1) with three-field functional, we get

$$\prod_{\mathbf{EAS}}(\mathbf{u},\tilde{\boldsymbol{\varepsilon}},\boldsymbol{\sigma}) = \int_V \left[\frac{1}{2}(\mathbf{B}\mathbf{u}+\tilde{\boldsymbol{\varepsilon}})\mathbf{C}(\mathbf{B}\mathbf{u}+\tilde{\boldsymbol{\varepsilon}}) - \boldsymbol{\sigma}^{\mathbf{T}}\tilde{\boldsymbol{\varepsilon}}\right] \mathrm{d}V \quad - \int_V \mathbf{u}^{\mathbf{T}}\bar{\mathbf{b}}\,\mathrm{d}V - \int_{S_\sigma} \mathbf{u}^{\mathbf{T}}\bar{\mathbf{t}}\,\mathrm{d}S - \int_{S_u} \mathbf{t}^{\mathbf{T}}(\mathbf{u}-\bar{\mathbf{u}})\,\mathrm{d}S \tag{3}$$

The Euler equations for the stationarity of this functional Eq. (3), in which boundary condition and force term is removed, are

$$\int_V \delta\mathbf{u}^{\mathbf{T}}\mathbf{B}^{\mathbf{T}}[\mathbf{C}(\mathbf{B}\mathbf{u}+\tilde{\boldsymbol{\varepsilon}})]\,\mathrm{d}V = 0 \tag{4}$$

$$\int_V \delta\boldsymbol{\sigma}^{\mathbf{T}}\tilde{\boldsymbol{\varepsilon}}\,\mathrm{d}V = 0 \tag{5}$$

$$\int_V \delta\tilde{\boldsymbol{\varepsilon}}^{\mathbf{T}}[\mathbf{C}(\mathbf{B}\mathbf{u}+\tilde{\boldsymbol{\varepsilon}}) - \boldsymbol{\sigma}]\,\mathrm{d}V = 0 \tag{6}$$

Fig. 1 shows the assumed displacements of a typical isoparametric eight-node solid element on the global and natural coordinate system. The enhanced assumed strain, defined in the global coordinate, is interpolated according to Eq. (2)

$$\tilde{\boldsymbol{\varepsilon}} = \mathbf{M}\boldsymbol{\alpha} \tag{7}$$

$$\mathbf{M} = \frac{\det\mathbf{J}_\mathbf{0}}{\det\mathbf{J}}\mathbf{T}_\mathbf{0}^{-\mathbf{T}}\mathbf{M}_{\boldsymbol{\xi}} \tag{8}$$

where $\det\mathbf{J}$ denotes the determinant of the Jacobian matrix $\mathbf{J}$, $\det\mathbf{J}_\mathbf{0}$ is the determinant of the Jacobian matrix $\mathbf{J}_\mathbf{0} = \mathbf{J}|_{\xi=\eta=\zeta=0}$ at center ($\xi=\eta=\zeta=0$) of the element in the natural coordinate, and $\mathbf{M}_{\boldsymbol{\xi}}$ is the shape or interpolation function for the enhanced assumed strain, respectively.

According to tensor calculus, $\mathbf{T}_\mathbf{0}^{-\mathbf{T}}$ maps the polynomial shape functions of $\mathbf{M}_{\boldsymbol{\xi}}$, defined in the natural coordinate, into the global coordinate (Simo and Rifai, 1990). This transformation is restricted to the origin so that the components of $\mathbf{T}_\mathbf{0}^{-\mathbf{T}}$ are constant and the chosen polynomial order is not increased. Then the matrix $\mathbf{T}_\mathbf{0}^{-\mathbf{T}}$ contains the components J_{ij_0} of $\mathbf{J}_\mathbf{0}$ and can be written as

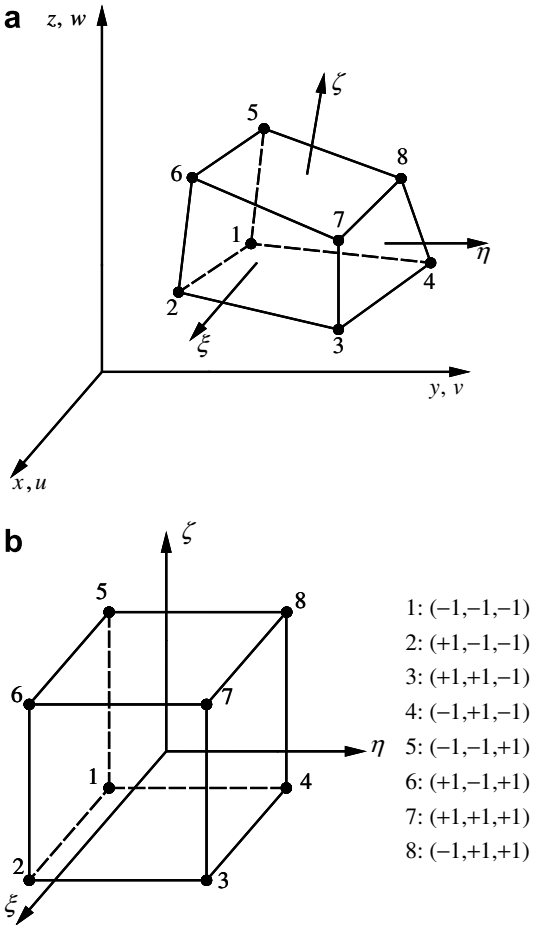

Fig. 1. Assumed displacements of a typical isoparametric eight-node solid element on the global (Cartesian) and natural coordinate system. (a) Global coordinate system. (b) Natural coordinate system.

$$\mathbf{T_0} = \begin{bmatrix} J_{11_0}^2 & J_{21_0}^2 & J_{31_0}^2 & 2J_{11_0}J_{21_0} & 2J_{21_0}J_{31_0} & 2J_{11_0}J_{31_0} \\ J_{12_0}^2 & J_{22_0}^2 & J_{32_0}^2 & 2J_{12_0}J_{22_0} & 2J_{22_0}J_{32_0} & 2J_{12_0}J_{32_0} \\ J_{13_0}^2 & J_{23_0}^2 & J_{33_0}^2 & 2J_{13_0}J_{23_0} & 2J_{23_0}J_{33_0} & 2J_{13_0}J_{33_0} \\ J_{11_0}J_{12_0} & J_{21_0}J_{22_0} & J_{31_0}J_{32_0} & J_{11_0}J_{22_0}+J_{21_0}J_{12_0} & J_{21_0}J_{32_0}+J_{31_0}J_{22_0} & J_{11_0}J_{32_0}+J_{31_0}J_{12_0} \\ J_{12_0}J_{13_0} & J_{22_0}J_{23_0} & J_{32_0}J_{33_0} & J_{12_0}J_{23_0}+J_{22_0}J_{13_0} & J_{22_0}J_{33_0}+J_{32_0}J_{23_0} & J_{12_0}J_{33_0}+J_{32_0}J_{13_0} \\ J_{11_0}J_{13_0} & J_{21_0}J_{23_0} & J_{31_0}J_{33_0} & J_{11_0}J_{23_0}+J_{21_0}J_{13_0} & J_{21_0}J_{33_0}+J_{31_0}J_{23_0} & J_{11_0}J_{33_0}+J_{31_0}J_{13_0} \end{bmatrix} \tag{9}$$

where J_{ij_0} are the components of Jacobian matrix $\mathbf{J_0}$ at the center of the element in the natural coordinate. The Jacobian matrix at the center of the element ($\xi = \eta = \zeta = 0$) does not originate the unexpected strain energy by the enhanced strain. The revised Jacobian at center of element then guarantees that the patch test is passed.

In Eq. (8), $\mathbf{M}_{\xi}$ must be assumed by the linear independent interpolation functions that satisfy the orthogonality of Eq. (5) (Simo and Rifai, 1990). Therefore, an optimal interpolation of $\mathbf{M}_{\xi}$ for the enhanced assumed strain can be found by inspecting the polynomial field of the compatible strain in the natural coordinate system. In order to decouple and enhance compatible strains, following complete trilinear 30-parameters interpolation function in the natural coordinate was chosen (Andelfinger and Ramm, 1993)

$$\mathbf{M}_{\xi}=\left[\begin{array}{ccc|cccccc|cccccc}
\xi & 0 & 0 & 0 & 0 & 0 & 0 & 0 & 0 & 0 & 0 & 0 & 0 & 0 & 0 \\
0 & \eta & 0 & 0 & 0 & 0 & 0 & 0 & 0 & 0 & 0 & 0 & 0 & 0 & 0 \\
0 & 0 & \zeta & 0 & 0 & 0 & 0 & 0 & 0 & 0 & 0 & 0 & 0 & 0 & 0 \\
0 & 0 & 0 & \xi & \eta & 0 & 0 & 0 & 0 & \xi\zeta & \eta\zeta & 0 & 0 & 0 & 0 \\
0 & 0 & 0 & 0 & 0 & \eta & \zeta & 0 & 0 & 0 & 0 & \xi\eta & \xi\zeta & 0 & 0 \\
0 & 0 & 0 & 0 & 0 & 0 & 0 & \xi & \zeta & 0 & 0 & 0 & 0 & \xi\eta & \eta\zeta
\end{array}\right.$$

$$\left.\begin{array}{cccccc|ccc|ccc|ccc}
\xi\eta & \xi\zeta & 0 & 0 & 0 & 0 & 0 & 0 & 0 & \xi\eta\zeta & 0 & 0 & 0 & 0 & 0 \\
0 & 0 & \xi\eta & \eta\zeta & 0 & 0 & 0 & 0 & 0 & 0 & \xi\eta\zeta & 0 & 0 & 0 & 0 \\
0 & 0 & 0 & 0 & \xi\zeta & \eta\zeta & 0 & 0 & 0 & 0 & 0 & \xi\eta\zeta & 0 & 0 & 0 \\
0 & 0 & 0 & 0 & 0 & 0 & \xi\eta & 0 & 0 & 0 & 0 & 0 & \xi\eta\zeta & 0 & 0 \\
0 & 0 & 0 & 0 & 0 & 0 & 0 & \eta\zeta & 0 & 0 & 0 & 0 & 0 & \xi\eta\zeta & 0 \\
0 & 0 & 0 & 0 & 0 & 0 & 0 & 0 & \xi\zeta & 0 & 0 & 0 & 0 & 0 & \xi\eta\zeta
\end{array}\right]. \tag{10}$$

2.2. Finite element formulation

2.2.1. Element stiffness matrix

Eqs. (7) and (8) are introduced into the energy principle of Eq. (3), and variation with respect to the unknown parameters $\mathbf{d}_i$ and $\boldsymbol{\alpha}_i$ results in the following system of equations:

$$\begin{bmatrix}\mathbf{K_{CC}} & \mathbf{K_{CN}} \\ \mathbf{K_{CN}^T} & \mathbf{K_{NN}}\end{bmatrix}^e \begin{bmatrix}\mathbf{d}_i \\ \boldsymbol{\alpha}_i\end{bmatrix}^e = \begin{bmatrix}\mathbf{F} \\ \mathbf{0}\end{bmatrix}^e \tag{11}$$

where $\mathbf{F}$ is the vector of applied nodal forces used in the displacement method, $\mathbf{d}_i$ is the nodal displacements of node i in the global coordinate system, and the stiffness matrix $\mathbf{K_{CC}}$, $\mathbf{K_{CN}}$, $\mathbf{K_{NN}}$ are described as

$$\begin{aligned}
\mathbf{K_{CC}} &= \int_V \mathbf{B^T Q B}\,\mathrm{d}V = \int_{-1}^{1}\int_{-1}^{1}\int_{-1}^{1} \mathbf{B^T Q B}|\mathbf{J}|\,\mathrm{d}\xi\,\mathrm{d}\eta\,\mathrm{d}\zeta \\
\mathbf{K_{CN}} &= \int_V \mathbf{B^T Q M}\,\mathrm{d}V = \int_{-1}^{1}\int_{-1}^{1}\int_{-1}^{1} \mathbf{B^T Q M}|\mathbf{J}|\,\mathrm{d}\xi\,\mathrm{d}\eta\,\mathrm{d}\zeta \\
\mathbf{K_{NN}} &= \int_V \mathbf{M^T Q M}\,\mathrm{d}V = \int_{-1}^{1}\int_{-1}^{1}\int_{-1}^{1} \mathbf{M^T Q M}|\mathbf{J}|\,\mathrm{d}\xi\,\mathrm{d}\eta\,\mathrm{d}\zeta
\end{aligned} \tag{12}$$

where the matrix $\mathbf{B}$ is the compatible strain–displacement relation matrix. $\mathbf{Q}$ is the material stiffness matrix as following:

$$\mathbf{Q} = \mathbf{T C T^T} \tag{13}$$

where, $\mathbf{C}$ is the material stiffness matrix in the material axis, and $\mathbf{T}$ is the transformation matrix that the stresses and strains on the material axis can be transformed to those of the structural axis. The stress–strain for the structural axis is obtained by

$$\boldsymbol{\sigma}_\mathbf{s} = \mathbf{T}\boldsymbol{\sigma}_\mathbf{m} = \mathbf{T C}\boldsymbol{\varepsilon}_\mathbf{m} = \mathbf{T C T^T}\boldsymbol{\varepsilon}_\mathbf{s} \tag{14}$$

Fig. 2 shows the relationship between the structural or problem axis (x–y–z) and the material axis (1–2–3) for a lamina. Finally the stress–strain relations for an orthotropic material in the structural axis can be also expressed as

$$\boldsymbol{\sigma}_\mathbf{s} = \begin{bmatrix}\sigma_{xx}\\ \sigma_{yy}\\ \sigma_{zz}\\ \sigma_{xy}\\ \sigma_{yz}\\ \sigma_{zx}\end{bmatrix} = \begin{bmatrix}Q_{11} & Q_{12} & Q_{13} & Q_{14} & 0 & 0\\ Q_{12} & Q_{22} & Q_{23} & Q_{24} & 0 & 0\\ Q_{13} & Q_{23} & Q_{33} & Q_{34} & 0 & 0\\ Q_{14} & Q_{24} & Q_{34} & Q_{44} & 0 & 0\\ 0 & 0 & 0 & 0 & Q_{55} & Q_{56}\\ 0 & 0 & 0 & 0 & Q_{56} & Q_{66}\end{bmatrix} \begin{bmatrix}\varepsilon_{xx}\\ \varepsilon_{yy}\\ \varepsilon_{zz}\\ \varepsilon_{xy}\\ \varepsilon_{yz}\\ \varepsilon_{zx}\end{bmatrix} = \mathbf{Q}\boldsymbol{\varepsilon}_\mathbf{s} \tag{15}$$

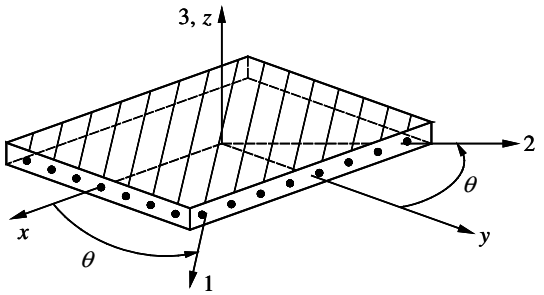

Fig. 2. A fiber-reinforced lamina with structure (x–y–z) and material (1–2–3) coordinate system ($+\theta$: counterclockwise).

Here, $\boldsymbol{\alpha}_i$ must be removed from Eq. (11), because it is an artificial parameter used for an enhanced strain. Then the static condensation for the strain parameter $\boldsymbol{\alpha}_i$ finally yields the element stiffness matrix as following:

$$\mathbf{K^e} = \mathbf{K_{CC}} - \mathbf{K_{CN}}\mathbf{K_{NN}^{-1}}\mathbf{K_{CN}^T} \tag{16}$$

2.2.2. Stress recovery

In order to obtain stresses in the EAS element, the hybrid formulation based on Hellinger–Reissner principle, e.g. HR-element, is used (Andelfinger and Ramm, 1993). This procedure is also the same as that of least-squares variation recovery (Simo and Rifai, 1990), provided that the same stress interpolation matrix is used in both procedures. The HR-formulation with continuous displacement and discontinuous stress fields can be summarized as follows:

$$\boldsymbol{\sigma}_e = \mathbf{P}\boldsymbol{\beta} = \mathbf{T_0}\mathbf{P}_\xi\boldsymbol{\beta} \tag{17}$$

$$\mathbf{H} = \int_V \mathbf{P^T}\mathbf{Q^{-1}}\mathbf{P}\,\mathrm{d}V \tag{18}$$

$$\mathbf{G} = \int_V \mathbf{P^T}\mathbf{B}\,\mathrm{d}V \tag{19}$$

$$\boldsymbol{\sigma}_e = \mathbf{P}\mathbf{H^{-1}}\mathbf{G}\mathbf{u}_e \tag{20}$$

for all elements $e = 1, 2, \ldots, n_{\text{elem}}$

where, $\mathbf{P}_\xi$ is the interpolation function matrix for stresses in the natural coordinates, $\mathbf{u}_e$ is the displacement vector on element, and $\boldsymbol{\sigma}_e$ are the stresses at each gauss integration points on the element. The stiffness matrix of the HR-element based on the Hellinger–Reissner principle is equivalent to the stiffness matrix of the EAS-element, if polynomials in $\mathbf{M}_\xi$ and $\mathbf{P}_\xi$ are complementary. In addition, the components of $\mathbf{M}_\xi$ and $\mathbf{P}_\xi$ must be independent each other. In other words, if $\mathbf{S^M}$ is the n-dimensional space of the polynomial expansion in $\mathbf{M}_\xi$ and $\mathbf{S^P}$ that corresponding to $\mathbf{P}_\xi$, the following two conditions must hold for this equivalence

$$\mathbf{S^M} \cup \mathbf{S^P} = \mathbf{S}^{\text{complete}} \tag{21}$$

$$\mathbf{S^M} \cap \mathbf{S^P} = \emptyset \tag{22}$$

For a trilinear element, for example, the eight-node solid element $\mathbf{S}^{\text{complete}}$ defines the six-dimensional space with complete trilinear polynomials. The stresses of the EAS- and HR-element are also identical if the stresses for the EAS-element are calculated according to the HR-formula as

$$\boldsymbol{\sigma}_e = \mathbf{P}\mathbf{H^{-1}}\mathbf{G}\mathbf{u}_e \tag{23}$$

These stresses always satisfy Eq. (5). By substituting Eq. (23) into Eq. (5) and exception of $\mathbf{P}_\xi$ and $\mathbf{M}_\xi$, all other terms are constant so that

$$\int_{-1}^{1}\int_{-1}^{1}\int_{-1}^{1} \mathbf{P}_\xi^{\mathbf{T}}\mathbf{M}_\xi\,\mathrm{d}\xi\,\mathrm{d}\eta\,\mathrm{d}\zeta = 0 \tag{24}$$

In order to satisfy Eqs. (21), (22) and (24), $\mathbf{P}_\xi$ in the natural coordinates must be assumed as

$$\mathbf{P}_\xi = \begin{bmatrix} 1 & \eta & \zeta & \eta\zeta & 0 & 0 & 0 & 0 & 0 & 0 & 0 & 0 & 0 & 0 & 0 & 0 & 0 & 0 \\ 0 & 0 & 0 & 0 & 1 & \xi & \zeta & \xi\zeta & 0 & 0 & 0 & 0 & 0 & 0 & 0 & 0 & 0 & 0 \\ 0 & 0 & 0 & 0 & 0 & 0 & 0 & 0 & 1 & \xi & \eta & \xi\eta & 0 & 0 & 0 & 0 & 0 & 0 \\ 0 & 0 & 0 & 0 & 0 & 0 & 0 & 0 & 0 & 0 & 0 & 0 & 1 & \zeta & 0 & 0 & 0 & 0 \\ 0 & 0 & 0 & 0 & 0 & 0 & 0 & 0 & 0 & 0 & 0 & 0 & 0 & 0 & 1 & \xi & 0 & 0 \\ 0 & 0 & 0 & 0 & 0 & 0 & 0 & 0 & 0 & 0 & 0 & 0 & 0 & 0 & 0 & 0 & 1 & \eta \end{bmatrix} \tag{25}$$

The stresses obtained by the Eq. (23) are the stresses (σ_{1-8}) at gauss integration points of each eight-node solid element. In order to obtain the stresses at the nodal point, the extrapolation method is used. The stresses (σ_{A-H}) at the nodal point of each eight-node solid element can be calculated by Eq. (26).

$$\begin{bmatrix} \sigma_A \\ \sigma_B \\ \sigma_C \\ \sigma_D \\ \sigma_E \\ \sigma_F \\ \sigma_G \\ \sigma_H \end{bmatrix} = \frac{1}{8} \begin{bmatrix} 10+6\sqrt{3} & -2-2\sqrt{3} & -2+2\sqrt{3} & -2-2\sqrt{3} & -2-2\sqrt{3} & -2+2\sqrt{3} & 10-6\sqrt{3} & -2+2\sqrt{3} \\ & 10+6\sqrt{3} & -2-2\sqrt{3} & -2+2\sqrt{3} & -2+2\sqrt{3} & -2-2\sqrt{3} & -2+2\sqrt{3} & 10-6\sqrt{3} \\ & & 10+6\sqrt{3} & -2-2\sqrt{3} & 10-6\sqrt{3} & -2+2\sqrt{3} & -2-2\sqrt{3} & -2+2\sqrt{3} \\ & & & 10+6\sqrt{3} & -2+2\sqrt{3} & 10-6\sqrt{3} & -2+2\sqrt{3} & -2-2\sqrt{3} \\ & & & & 10+6\sqrt{3} & -2-2\sqrt{3} & -2+2\sqrt{3} & -2-2\sqrt{3} \\ & & & & & 10+6\sqrt{3} & -2-2\sqrt{3} & -2+2\sqrt{3} \\ & & & & & & 10+6\sqrt{3} & -2-2\sqrt{3} \\ \text{symmetry} & & & & & & & 10+6\sqrt{3} \end{bmatrix} \begin{bmatrix} \sigma_1 \\ \sigma_2 \\ \sigma_3 \\ \sigma_4 \\ \sigma_5 \\ \sigma_6 \\ \sigma_7 \\ \sigma_8 \end{bmatrix} \tag{26}$$

In this study, the finite element obtained by these procedures is named by "EAS-SOLID8".

2.3. Buckling analysis

The buckling behavior of the laminated composite structures is very important for the design of civil engineering structures. In this study, the finite element method is used to investigate the buckling behavior of the described analysis model. The basic equation of buckling analysis in the form of an eigenproblem is

$$\mathbf{K}^{\mathbf{e}}\boldsymbol{\phi} = \lambda \mathbf{K}_{\mathbf{G}}\boldsymbol{\phi} \tag{27}$$

where $\mathbf{K}^{\mathbf{e}}$ and $\mathbf{K}_{\mathbf{G}}$ are the elastic and geometric stiffness matrices of the structure, respectively, and $\boldsymbol{\phi}$ is the generalized global displacement vector. The elastic stiffness matrix $\mathbf{K}$ is defined by Eq. (16). This eigenproblem is solved by the subspace iteration procedure that is an effective method widely used in engineering practice for the solution of eigenvalues and eigenvectors of finite element equations. This technique is particularly suited for the calculation of a few eigenvalues and eigenvectors of large finite element system. The subspace iteration method is developed by Bathe (1996). The smallest eigenvalue λ_1 among eigenvalues obtained by the subspace iteration method is the buckling load N_{cr}, and its corresponding eigenvector ϕ_1 represents the buckling mode for the buckling load, the smallest eigenvalue.

The geometric stiffness matrix $\mathbf{K}_{\mathbf{G}}$ of the eight-node solid element must be formulated for the eigenproblem. If the in-plane loads are applied in x- or y-direction for an infinitesimal solid element on the structural element, the infinitesimal solids element, as shown in Fig. 3, will be buckled to z-direction. In this case, the geometric stiffness matrix $\mathbf{K}_{\mathbf{G}}$ for the eight-node solid element that is expressed by the standard shape function of equation is described as

$$\mathbf{K}_{\mathbf{G}} = \int_V \mathbf{B}_{\mathbf{G}}^{\mathbf{T}} \bar{\mathbf{N}} \mathbf{B}_{\mathbf{G}} \, \mathrm{d}V = \int_{-1}^{1}\int_{-1}^{1}\int_{-1}^{1} \mathbf{B}_{\mathbf{G}}^{\mathbf{T}} \bar{\mathbf{N}} \mathbf{B}_{\mathbf{G}} |\mathbf{J}| \, \mathrm{d}\xi \, \mathrm{d}\eta \, \mathrm{d}\zeta \tag{28}$$

where $\bar{\mathbf{N}}$ means in-plane force vector as shown in Fig. 3 and $\mathbf{B}_{\mathbf{G}}$ is the derivative matrix of the shape function in Eq. (29).

$$\mathbf{B}_{\mathbf{G}} = \begin{bmatrix} 0 & 0 & \frac{\partial \mathbf{N}_i}{\partial x} \\ 0 & 0 & \frac{\partial \mathbf{N}_i}{\partial y} \end{bmatrix} = \mathbf{J}^{-1} \begin{bmatrix} 0 & 0 & \frac{\partial \mathbf{N}_i}{\partial \xi} \\ 0 & 0 & \frac{\partial \mathbf{N}_i}{\partial \eta} \end{bmatrix}, \quad i = 1\text{–}8 \tag{29}$$

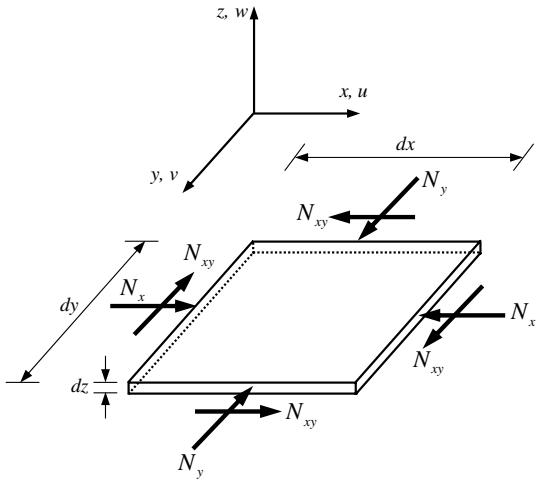

Fig. 3. Infinitesimal solid element under in-plane load.

$$\bar{\mathbf{N}} = \begin{bmatrix} N_x & N_{xy} \\ N_{xy} & N_y \end{bmatrix} \tag{30}$$

where $\mathbf{N}_i$ ($i = 1$–8) is the shape function of a typical isoparametric eight-node solid element in the natural coordinate system and Eq. (30) must be transformed into Eq. (31) because in this study the unidirectional uniform in-plane loading in x-direction is only considered.

$$\bar{\mathbf{N}} = \begin{bmatrix} 1.0 & 0.0 \\ 0.0 & 0.0 \end{bmatrix} \tag{31}$$

3. Numerical examples

3.1. Numerical verification

The isoparametric eight-node solid element with an enhanced assumed strain used in this study is compared with the bench mark test proposed by other researchers. In order to evaluate the performance of the proposed solid elements, the patch test, distortion test, and other various numerical tests are carried out. The examples carried out in this chapter are given to demonstrate the efficiency and accuracy of the proposed solid element.

3.1.1. Eigenvalue test

In order to test the behavior of solid elements in the nearly incompressible range, an eigenvalue analysis is performed for one square element with a side length 1.0 and $E = 1.0$. The material is assumed to be incompressible, i.e. in the numerical calculation $v = 0.4999$ was used, rendering eigenvalues of 10^3–10^5 instead of ∞. Table 1 shows the eigenvalues for 18 modes; the six zero-eigenvalues for the six rigid body modes are not shown. The proposed element and HR-element, which has equivalence with the proposed element, give the correct eigenvalues. The HR-18 element proposed by Pian (1982) is an eight-node hybrid element used by 18 parameters for the stress assumption.

In Table 1, for a volumetric-locking free behavior, it is important that elements contain only one incompressible mode; i.e. its eigenvalue is infinite. For the displacement model DISP, standard eight-node solid element, six deviatoric modes are always mixed up by parasitic volumetric strains when for $v = 0.5$ leads to six unrealistic infinite eigenvalues.

Table 1
Eigenvalues for eight-node solid elements with an incompressible material (the six zero eigenvalues are not shown)

	DISP	HR-18 (Pian, 1982)	EAS-SOLID8
1	0.0555	0.0555	0.0555
2	0.0555	0.0555	0.0555
3	0.1666	0.0555	0.0555
4	0.1666	0.0555	0.0555
5	0.1666	0.0555	0.0555
6	0.2222	0.1111	0.1111
7	0.3333	0.1111	0.1111
8	0.3333	0.1111	0.1111
9	0.3333	0.2222	0.2222
10	0.3333	0.3333	0.3333
11	0.3333	0.3333	0.3333
12	∞	0.3333	0.3333
13	∞	0.3333	0.3333
14	∞	0.3333	0.3333
15	∞	0.3333	0.3333
16	∞	0.3333	0.3333
17	∞	0.3333	0.3333
18	∞	∞	∞

DISP, standard isoparametric eight-node solid element; HR-18, eight-node hybrid element used by 18 parameters for stress assumption.

3.1.2. Comparison of EAS and other elements

The cantilever beam presented in Figs. 4 and 5 is used to evaluate the performance of the two-dimensional hybrid element proposed by Pian and Sumihara (1984), three-dimensional hybrid element proposed by Cheung and Chen (1988), and three-dimensional incompatible element proposed by Wilson and Ibrahimbegovic (1990). In this study, the same example is used to demonstrate that the same accuracy can be obtained with the hybrid stress recovery method proposed in this study. The end moment and end shear are considered as applied loads. The same distorted mesh is used as the one presented in Pian and Sumihara (1984) and Cheung and Chen (1988). Both the displacement at point "B" and the normal stress (σ_x) at point "A" under the two load cases are compared with hybrid, incompatible, and compatible elements, and presented in Tables 2 and 3. In addition, results obtained by the solid element with incompatible modes given in Wu et al. (1987) and Wilson and Ibrahimbegovic (1990) are presented for comparison. Generally, it is known that the performance of the incompatible element is similar to that of the EAS element. In the case of the distorted mesh, Table 2, it is interesting to notice that the present formulation gives nearly the same results as the ones obtained by the incompatible element proposed by Wilson and Ibrahimbegovic (1990) and by the hybrid element proposed by Pian and Sumihara (1984). However, in the case of the trapezoidal mesh, Table 3, the present results for vertical displacement of this example are superior to the results of solid element with incompatible modes proposed by Wilson and Ibrahimbegovic (1990) and with compatible modes. Therefore, the performance of the EAS element is largely improved than that of the incompatible element.

3.1.3. Accuracy of stress recovery

The same cantilever beam shown in Fig. 5 is used to evaluate the performance of the element when the mesh of trapezoidal elements is selected. It was shown in Macneal (1987) that such a choice will bring about the locking phenomenon for any element which passes the patch test. Both the displacement at point "B" and the normal stress (σ_x) at point "A" under the two load cases is compared with other elements, and presented in Tables 2 and 3. Tip displacements for both load cases are approximately 20% smaller than the exact solution. However, although elements have the trapezoidal shape, the difference between computed and exact displacements is less than 2%. It can be also observed that the stress computed using the EAS-Solids8 is more accurate than those of the solid element with the incompatible modes proposed by Wilson and Ibrahimbegovic (1990).

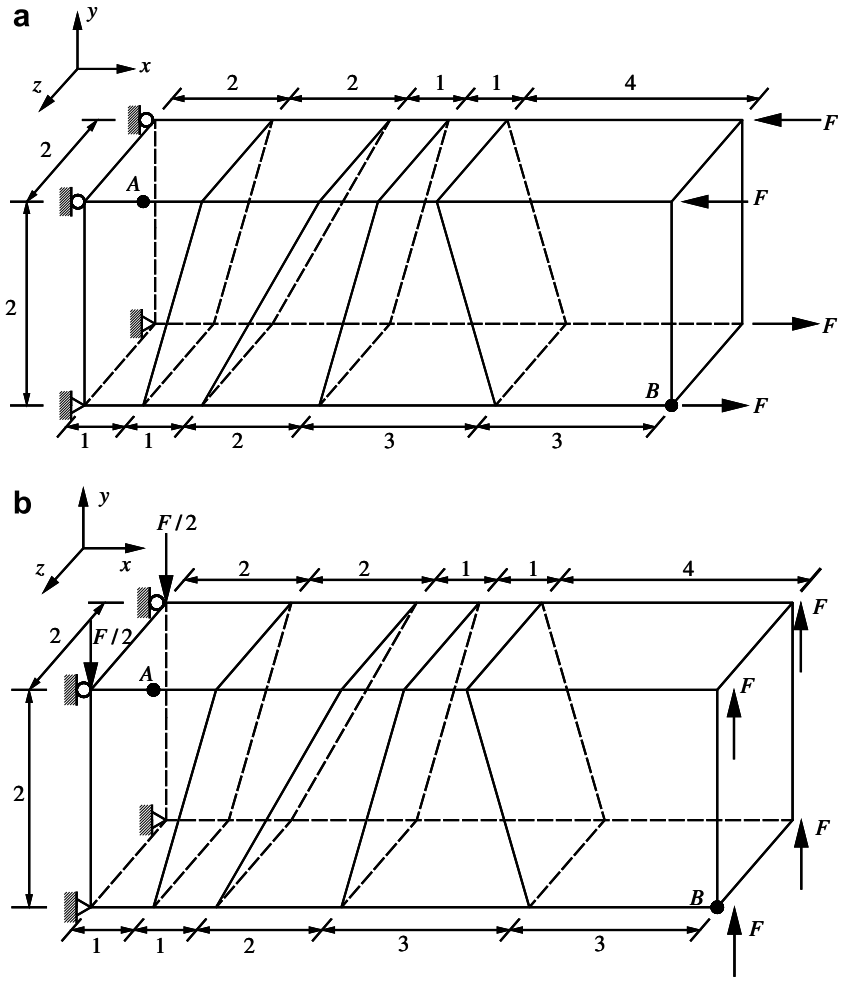

Fig. 4. Short cantilever beam with distorted mesh under moment and shear load ($E = 1500$, $v = 0.25$, point A, normal stress; point B, vertical displacement). (a) Moment load ($F = 1000$). (b) Shear load ($F = 150$).

3.1.4. Laminates without delaminations

The simply supported [0/90/90/0] cross-ply square laminated plates under uniform in-plane forces is considered for illustrating accuracy of buckling behavior by the EAS-SOLID8 elements. Individual layers are considered as the orthotropic material properties; $E_{11}/E_{22} = \text{open}$, $E_{22} = E_{33}$, $G_{12} = G_{13} = 0.6E_{22}$, $G_{23} = 0.5E_2$, $v_{12} = v_{13} = v_{23} = 0.25$. The nondimensionalized critical buckling loads with respect to various values of E_{11}/E_{22} are shown in Table 4 and are compared with the three-dimensional elasticity solution given by Noor (1975). The present results show some larger values than all other theories and have accurate values within 4% with respect to 3D elasticity solution. The nondimensionalized critical buckling loads with respect to various values of a/h are also shown in Table 5. In Table 5, the present results also show accurate values with respect to all other theories. The present results show the smallest buckling loads, specially for $a/h = 4$. The difference between all the theories is a minimum for very thin laminates whereas EAS-SOLID8 shows the smallest buckling loads with respect to other theories for thick laminates. It should be pointed out from the tables that the EAS-SOLID8 demonstrates excellent performance in a buckling problem of laminates with not only thick but also thin thickness for various material properties.

3.1.5. Laminates with delaminations

Four-layer square laminate [0//0/0/0] with an embedded circular delamination on the buckling behavior of composite laminate as shown in Fig. 6 is considered to compare the present study with CLT, FSDT,

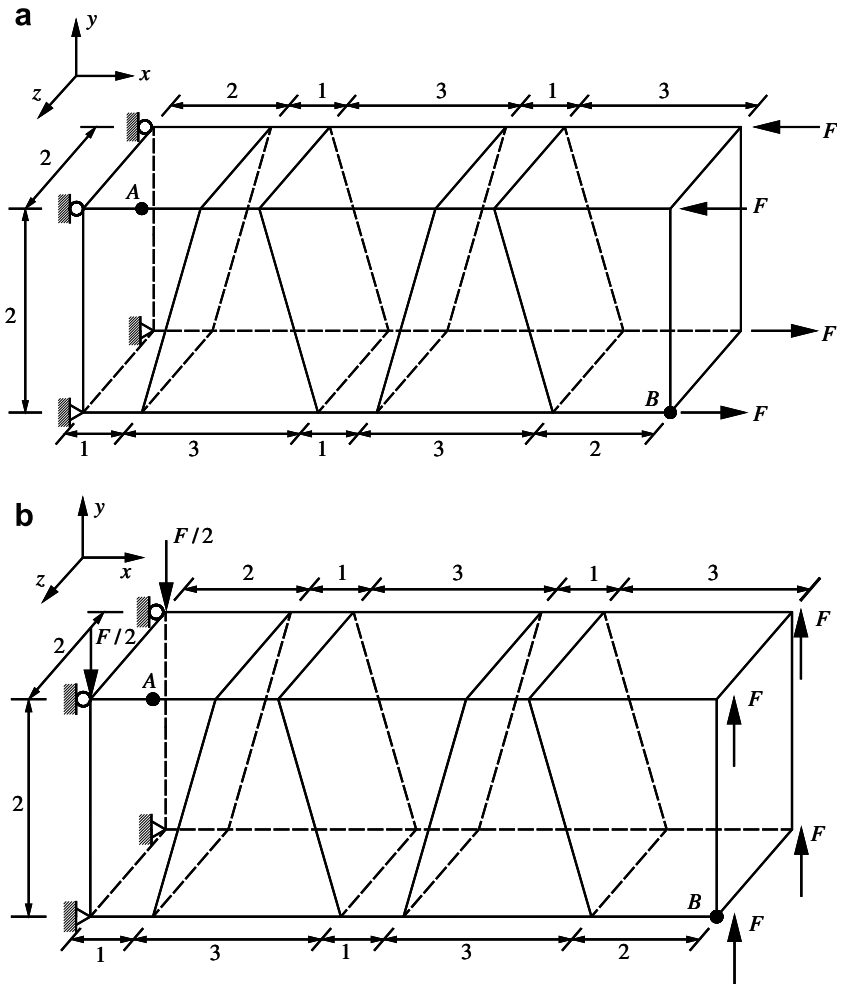

Fig. 5. Short cantilever beam with trapezoidal mesh under moment and shear load ($E = 1500$, $v = 0.25$, point A, normal stress; point B, vertical displacement). (a) Moment load ($F = 1000$). (b) Shear load ($F = 150$).

EHOPTWD, and Kim (1997). The double slash '//' represents the position of a delamination within the laminates. The laminate has length $L = 150$ mm and thickness $H = 4 \times 0.125$ mm. Material properties of the plate were given by

Table 2
Vertical displacement and stress of short cantilever beam – distorted mesh

Element	Load case	Vertical displacement (point B)	Normal stress (point A)
Pian and Sumihara (1984)	Moment	96.18 (−3.82)	−3014 (0.47)
Cheung and Chen (1988)	Moment	92.2 (−7.80)	−3006.6 (0.22)
Wu et al. (1987)	Moment	93.7 (−6.30)	−2484 (−17.2)
Wilson and Ibrahimbegovic (1990)	Moment	95.8 (−4.20)	−3015 (0.50)
EAS-SOLID8	Moment	95.98 (−4.02)	−3015 (0.50)
Exact solution		100.0	−3000
Pian and Sumihara (1984)	Shear	98.19 (−4.30)	−4137 (2.15)
Cheung and Chen (1988)	Shear	94.05 (−8.33)	−4125.3 (1.85)
Wilson and Ibrahimbegovic (1990)	Shear	97.9 (−4.58)	−4138.5 (2.19)
EAS-SOLID8	Shear	98.36 (−4.13)	−4146.3 (2.38)
Exact solution		102.6	−4050

Numbers in the parentheses are the percentage error with respect to exact solution.

Table 3
Vertical displacement and stress of short cantilever beam – trapezoidal mesh

Element	Load case	Vertical displacement (point B)	Normal stress (point A)
Compatible[#]	Moment	53.439 (−46.6)	−2720.5 (−9.3)
Compatible[*]	Moment	53.439 (−46.6)	−1473 (−50.9)
Wilson and Ibrahimbegovic (1990)	Moment	76.252 (−23.7)	−2883.5 (−3.9)
EAS-SOLID8	Moment	80.630 (−19.4)	−2977 (−0.8)
Exact solution		100.0	−3000
Compatible	Shear	57.728 (−43.7)	−3784 (−6.6)
Compatible[*]	Shear	57.728 (−43.7)	−2051 (−49.4)
Wilson and Ibrahimbegovic (1990)	Shear	80.115 (−21.9)	−3860 (−4.7)
EAS-SOLID8	Shear	85.636 (−16.5)	−4105 (1.4)
Exact solution		102.6	−4050 (0.00%)

Numbers in the parentheses are the percentage error with respect to Exact solution. [#]Stresses evaluated from stress recovery for standard solid element. [*]Stresses evaluated from the displacements of standard solid element.

$$E_{11} = 135.4\ \text{GPa}, \quad E_{22} = 9.6\ \text{GPa}, \quad E_{33} = E_{22},$$
$$G_{12} = G_{13} = 4.8\ \text{GPa}, \quad G_{23} = 3.2\ \text{GPa}, \quad v_{12} = v_{13} = v_{23} = 0.31 \tag{32}$$

Fig. 7 shows the effect of the delamination size and boundary conditions on the buckling loads. In this study, for a clamped support, the induced buckling loads show higher values for small delamination sizes ($D/L = 0.2$) when compared with those proposed by Kim (1997). On the other hand, the induced buckling loads show comparatively lower values as the delamination size increases. For a simple support, the induced buckling loads for $D/L < 0.4$ are in good agreement with those proposed by Kim (1997). However, it can be observed that the induced buckling loads show comparatively lower values than others as the delamination size increases. This is probably due to the fact that a complete three-dimensional model reveals local buckling at the smaller delamination area than other models that use two-dimensional plate elements. Moreover, the boundary condition modeled using the plate elements is inconsistent with that modeled using the solid elements employed in this study. Therefore, the three-dimensional model using solid elements employed in our analysis achieves better accuracy, particularly for laminated composite plates with small delamination area.

3.2. Parameter studies

In this study, the buckling analysis of the laminated composite plates with the through-the-width or embedded delaminations is accomplished by the full three-dimensional model using eight node solid elements with EAS fields. In order to investigate the buckling behavior of laminated composite plates with delamination, it is

Table 4
Nondimensionalized critical buckling coefficients $\bar{N}_x = N_x b^2/(E_{22}h^3)$ as a variation of E_{11}/E_{22} for simply supported [0/90/90/0] cross-ply square laminated plates

Source	Mesh	E_1/E_2				
		3	10	20	30	40
EAS-SOLID8	$4\times4\times4$	5.5225 (4.11)	10.2166 (4.66)	15.7576 (4.92)	20.2858 (5.09)	24.0764 (5.23)
	$8\times8\times4$	5.4422 (2.60)	10.0626 (3.08)	15.5336 (3.43)	20.0175 (3.70)	23.7793 (3.93)
	$10\times10\times4$	5.4326 (2.42)	10.0444 (2.89)	15.5071 (3.25)	19.9857 (3.53)	23.7440 (3.77)
3D Elasticity (Noor, 1975)		5.3044	9.7621	15.0191	19.3040	22.8807
Kant and Manjunatha (1988)	HSDT	5.3745 (1.32)	9.8066 (0.46)	14.8522 (−1.11)	18.8313 (−2.45)	22.0671 (−3.56)
Pandya and Kant (1988)	HSDT	5.3896 (1.61)	9.8319 (0.72)	14.8882 (−0.87)	18.8750 (−2.22)	22.1163 (−3.34)
Reddy (1984)	HSDT	5.3899 (1.61)	9.8325 (0.72)	14.8896 (−0.86)	18.8776 (−2.21)	22.1207 (−3.32)
Senthilnathan et al. (1987)	HSDT	5.4142 (2.07)	10.2133 (4.62)	16.2309 (8.07)	21.4288 (11.01)	25.9651 (13.48)
Whitney and Pagano (1970)	FSDT	5.3961 (1.73)	9.8711 (1.12)	14.9846 (−0.23)	19.0265 (−1.44)	22.3151 (−2.47)

Note. Numbers in the parentheses are the percentage errors with respect to 3D elasticity values.

Table 5
Nondimensionalized critical buckling coefficients $\bar{N}_x = N_x b^2/(E_{22}h^3)$ as a variation of a/h for simply supported [0/90/90/0] cross-ply square laminated plates

Source	Mesh	a/h				
		4	10	20	50	100
EAS-SOLID8	$4\times4\times4$	8.6632	24.0764	32.5460	36.2628	36.8715
	$8\times8\times4$	8.6139	23.7793	32.0111	35.5996	36.1858
	$10\times10\times4$	8.6135	23.7440	31.9479	35.5214	36.1050
Kant and Manjunatha (1988)	HSDT	8.8148	23.2527	31.6278	35.3409	35.9511
Pandya and Kant (1988d)	HSDT	8.8901	23.3026	31.6481	35.3448	35.9521
Reddy (1984)	HSDT	8.9822	23.3400	31.6596	35.3467	35.9526
Senthilnathan et al. (1987)	HSDT	10.6504	25.9651	32.9173	35.5981	36.0176
Whitney and Pagano (1970)	FSDT	9.1138	23.4529	31.7071	35.3560	35.9550

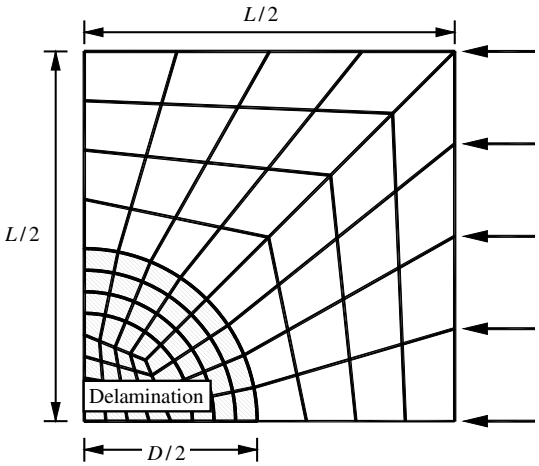

Fig. 6. A quarter mesh configuration of the laminated plates with embedded circular delaminations.

assumed that (1) the plates may be composed of layers of a single material or different materials, (2) the layers may be ordered in any sequence through the thickness, that is, the plate can be laminated symmetrically or unsymmetrically, and (3) the thickness of each layer is constant. Here, friction and contact conditions at delaminated interfaces are not considered and it is assumed that a delamination exists before loading and delamination growth is not considered. In this study, the parameter studies are all layers of equal thickness, and it is assumed that the delamination is located near the surface of the ply. The local or global buckling behaviors of laminated composite plates containing through-the-width or embedded delaminations are studied with various parameters, such as aspect ratio, width-to-thickness ratio, stacking sequences, and location of delamination and multiple delaminations.

3.2.1. Single through-the-width delamination

Fig. 8 shows the analysis model for laminated composite plates with through-the-width delamination. In Fig. 8, a and b are length of the plate in the x-direction and y-direction, respectively, h is the total thickness of the plate in the z-direction, and D is the size of the delamination in the x-direction. As shown in the figure, it is assumed that boundary conditions at two unloaded ends are free and at the two other ends are considered to be either clamped or simply supported, and the uniform in-plane load only in the x-direction of the plates is applied. As shown in Figs. 8(b) and (d), the quarter model is employed to investigate buckling behavior for cross-ply laminated composite plates with through-the-width delamination because the geometry of the plates

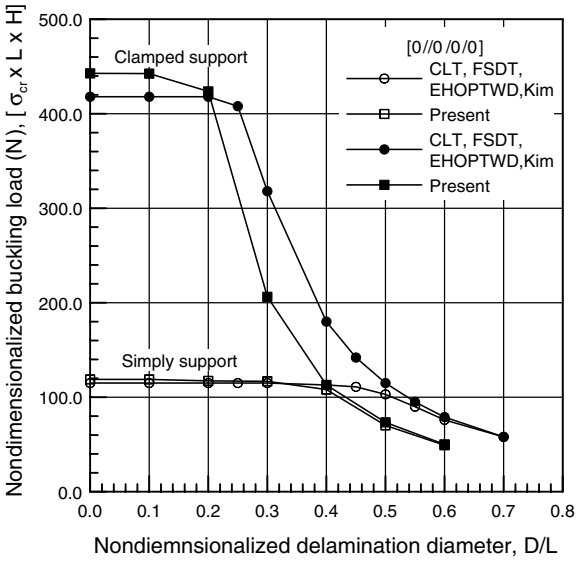

Fig. 7. Nondimensionalized buckling loads versus various nondimensionalized delamination sizes in [0//0/0/0] square orthotropic plates with embedded circular delaminations.

is symmetric. However, the whole model for angle-ply laminated composite plates is employed because the symmetric characteristics for the geometry of the plates are disappeared as shown in Figs. 8(a) and (c). The material properties applied for the all examples in this section are given as follows:

$$E_{11} = 25E_{22}, \quad E_{33} = E_{22}, \quad G_{12} = G_{13} = 0.5E_{22}, \quad G_{23} = 0.2E_{22}, \quad v_{12} = v_{23} = v_{13} = 0.25 \tag{33}$$

The obtained critical buckling stresses σ_{cr} are converted to critical buckling loads $\bar{N}_{cr}$, and then are nondimensionalized as Eq. (34)

$$\bar{N}_{cr} = (\sigma_{cr}/E_{22}) \times (b/h)^2 \tag{34}$$

3.2.1.1. Effect of aspect ratio. Fig. 9 shows the nondimensionalized buckling loads versus various aspect ratios (a/b) of the clamped supported [0//90/90/0] laminated plate with increased through-the-width delamination sizes (D/a). The buckling loads for $D/a = 0.8$ approach a constant value as the aspect ratio increases. On the other hand, the buckling load for small delamination sizes tends to decrease sharply within the same range. Fig. 10 shows the normalized buckling loads in the case without delamination shown in Fig. 9. From the figure, it can be observed that the induced buckling loads decreased drastically, particularly for $D/a > 0.2$. This phenomenon illustrates the fact that global buckling modes are changed into local buckling modes for small delamination sizes. Further, it can be observed that the local buckling mode starts more rapidly for larger aspect ratios.

3.2.1.2. Effect of width-to-thickness ratio. Fig. 11 shows the nondimensionalized buckling loads for different through-the-width delamination sizes of clamped [0//90/90/0] laminated square plate with various width-to-thickness ratios. From the figure, it can be seen that the buckling loads decrease sharply for $D/a \geqslant 0.2$ when a/h is 100, 40, and 20 (thin plate), while the buckling loads do not change significantly for $D/a \geqslant 0.3$ when a/h is 10 (thick plate). This can be attributed to the fact that the local buckling mode starts more rapidly for larger width-to-thickness ratios. For extremely large delamination sizes ($D/a = 0.8$), the buckling loads approach a constant value, regardless of the width-to-thickness ratios. This phenomenon is evident in Fig. 12. It is easy to understand that the extremely large delamination size results in a decrease in the plate resistance against the buckling behavior. Figs. 11 and 12 suggest that the influence of the delamination size may play certain roles in determining the buckling behavior of thin laminated composite plates. In particular, the thin plate with

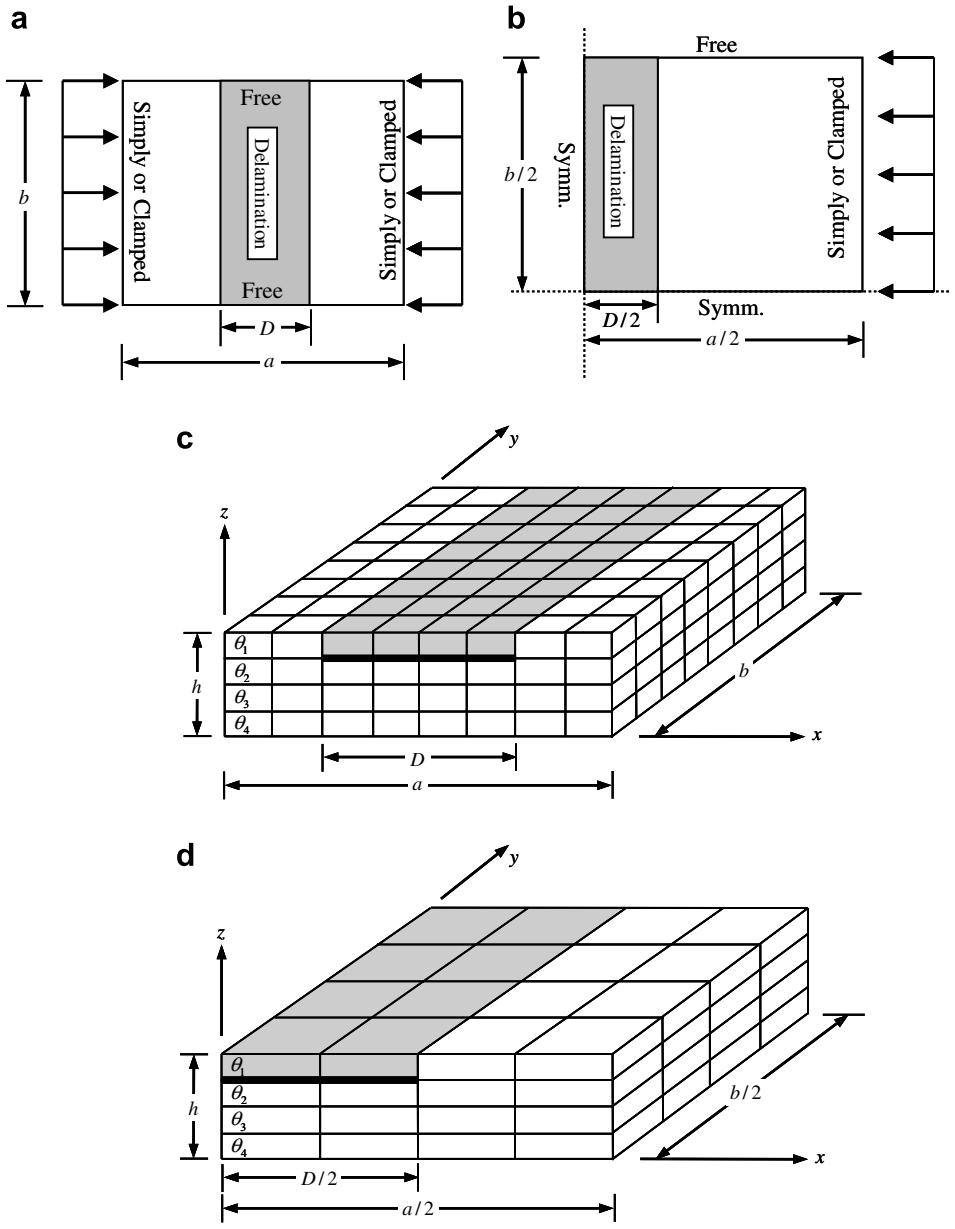

Fig. 8. Analysis model for laminated composite plates with through-the-width delamination. (a) Angle-ply laminates. (b) Cross-ply laminates. (c) Three-dimensional FE model for whole plate with angle-ply laminates. (d) Three-dimensional FE model for quarter plate with cross-ply laminates.

$D/a \geqslant 0.2$ is very sensitive to the buckling loads. Therefore, it is desirable to use the range of $D/a < 0.2$ for a reasonably stable design, as far as buckling is concerned.

3.2.1.3. Effect of stacking sequences. Fig. 13 shows the buckling loads for symmetric and antisymmetric cross-ply laminated square plates with different through-the-width delamination sizes (clamped boundaries). In Fig. 13, the symmetric [0//90/90/0] laminate exhibits the largest buckling loads. The buckling loads of the [90//0/90/0] and [90//0/0/90] laminates decrease sharply from $D/a \geqslant 0.1$, because the fiber orientation at the layer with the delamination is perpendicular to the in-plane loads. The ply angles result in worse rigidity

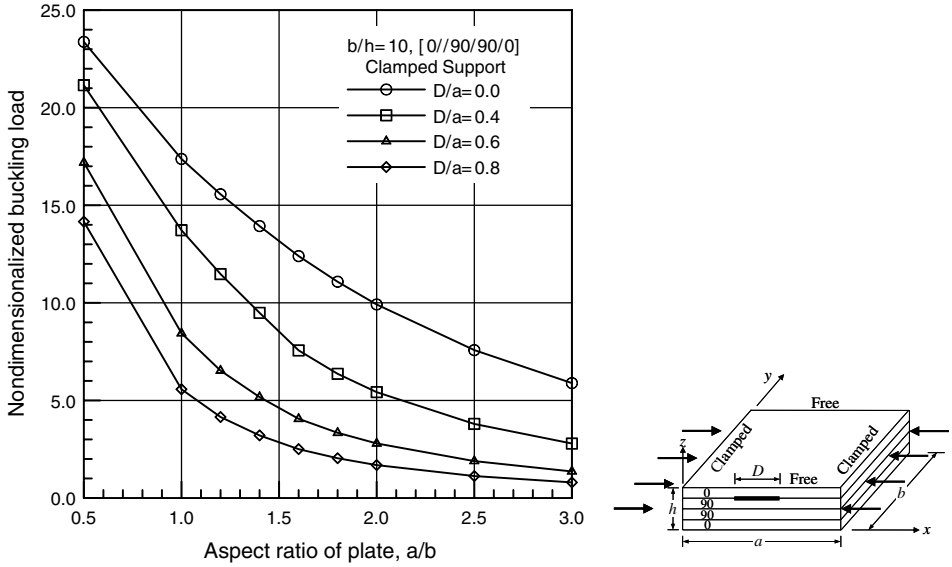

Fig. 9. Nondimensionalized buckling loads versus various aspect ratios of clamped [0//90/90/0] laminated plate with increased through-the-width delamination sizes; $b/h = 10$.

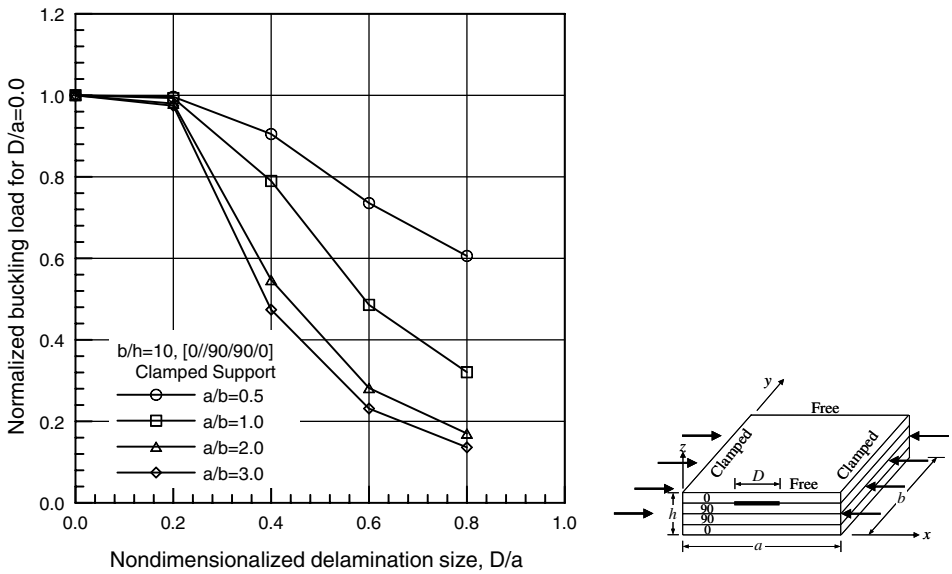

Fig. 10. Normalized buckling loads versus various through-the-width delamination sizes of clamped [0//90/90/0] laminated plate with various aspect ratios; $b/h = 10$.

against the buckling behavior. The local buckling modes occur suddenly for the [90//0/90/0] laminate because of the combined effects of the ply angle and delamination size.

Fig. 14 shows the buckling loads of the symmetric and antisymmetric angle-ply laminated square plates with different through-the-width delamination sizes (clamped boundaries). The fiber angles at each layer of the four-layered symmetric and antisymmetric composite plates are selected as 30°, 45°, and 60°. The induced buckling loads are significantly different for different fiber angles, because different fiber angles largely govern the changes in bending and shear stiffnesses. The buckling load of the [30//-30/30/-30] laminate exhibits the highest value. On the other hand, the differences in the buckling loads due to the layup sequence (symmetric

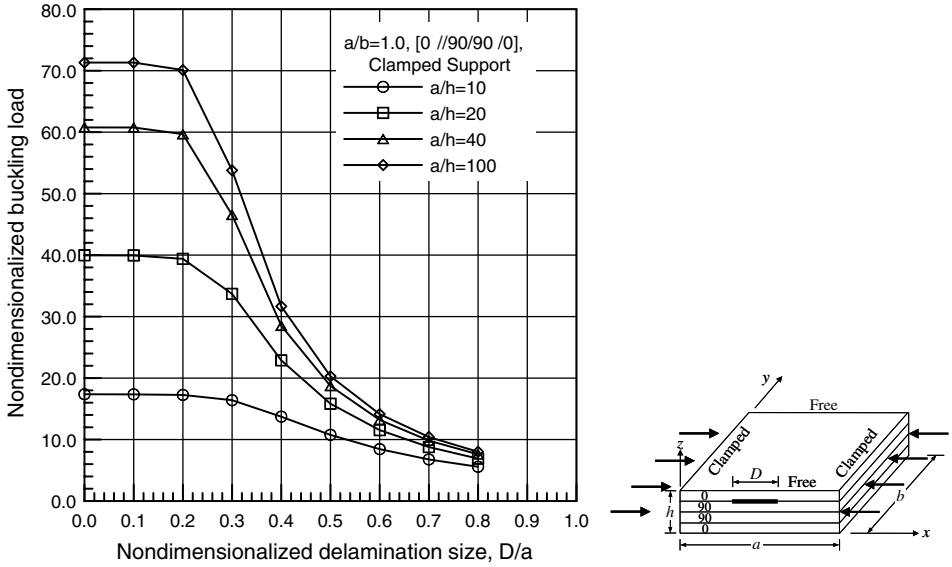

Fig. 11. Nondimensionalized buckling loads versus various through-the-width delamination sizes of clamped [0//90/90/0] laminated square plate with various width-to-thickness ratios; $a/b = 1.0$.

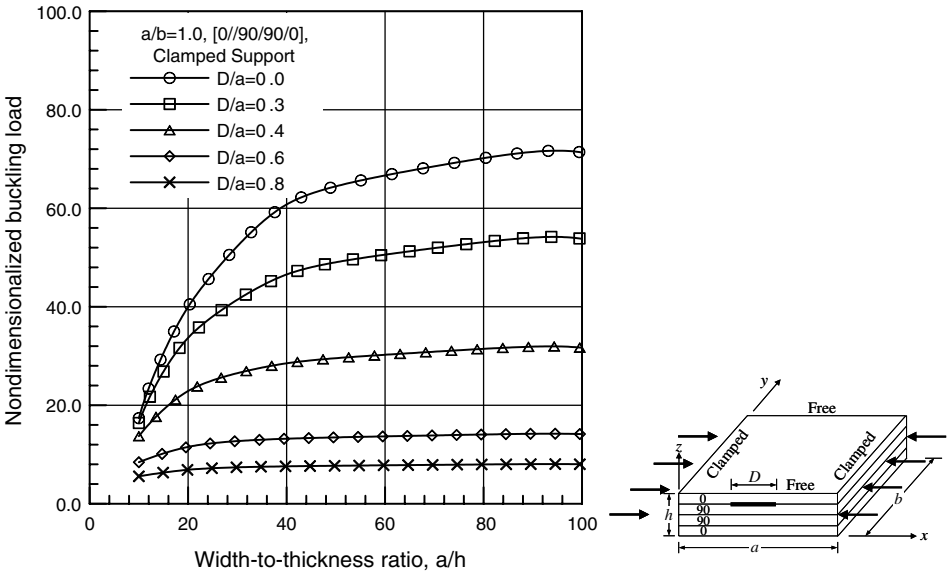

Fig. 12. Nondimensionalized buckling loads versus various width-to-thickness ratios of clamped [0//90/90/0] laminated square plate with various through-the-width delamination sizes; $a/b = 1.0$.

or antisymmetric) are negligible for $D/a \geqslant 0.2$; consequently, the buckling load does not change significantly. Figs. 15 and 16 show the global and local buckling mode shapes of a symmetric angle-ply laminated square plate with through-the-width single delamination. Small ply angles result in better rigidity and antisymmetric local buckling modes. As shown in these figures, some peculiar and complex mode shapes are induced due to the combined effect of both delamination size and fiber angle. In a two-dimensional buckling analysis using the existing plate element, the transition from the global to local buckling mode at the specific delamination area can not be accurately described as like Figs. 15 and 16. On the other hand, the three-dimensional dynamic analysis using a solid element can determine the buckling mode for an individual laminate face.

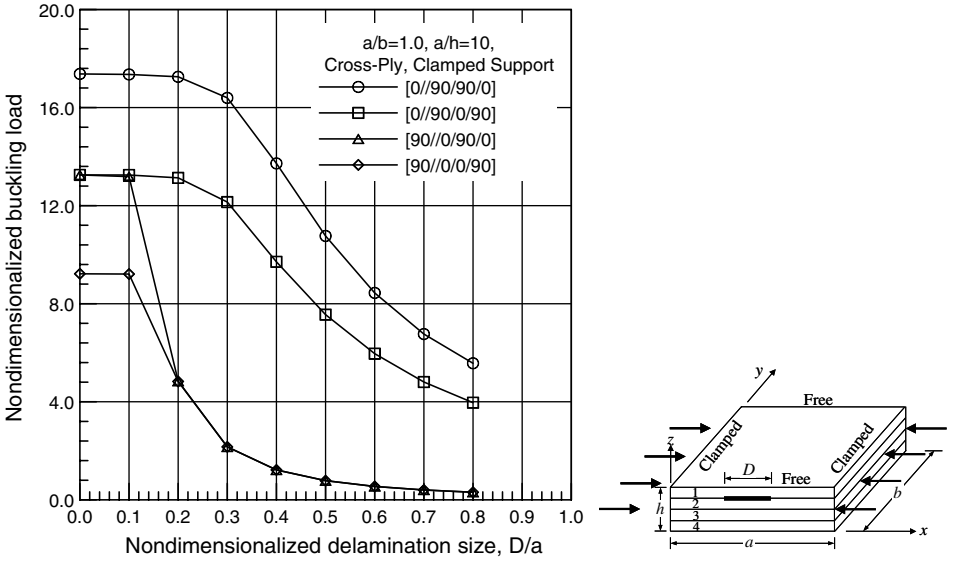

Fig. 13. Nondimensionalized buckling loads versus various through-the-width delamination sizes of clamped symmetric and antisymmetric cross-ply laminated square plates; $a/b = 1.0$, $a/h = 10$.

3.2.2. Multiple embedded delaminations

Figs. 17 and 18 show the nondimensionalized buckling loads for different delamination sizes of the clamped laminated square plates ($a/h = 10$) with various locations and number of delaminated layers for a symmetric cross-ply [0/90/90/0] laminate and an antisymmetric cross-ply [0/90/0/90] laminate, respectively. For symmetric case, as it is expected, we can observe (Fig. 17) that the buckling load decreases for an increased number of delaminations. However, the buckling load for different locations of delaminations is influenced by the fiber angles because of the same reason described earlier. Further, it can be observed that the change in the buckling loads for $D/a \leqslant 1.0$ is negligible, regardless of the size and location of delamination. For the antisymmetric case (shown in Fig. 18), the buckling load of the [0/90//0/90] laminate exhibits the highest value. In this case, we noted that the differences in the buckling loads due to the location and number of the delaminations show different trends when compared with the symmetric case. This is probably due to the effect of the coupling stiffness B_{ij}, which became nonzero for antisymmetric laminates, inducing complicated influences on the buckling behavior of the structural system.

4. Summary and conclusion

In this study, the solid finite element "EAS-SOLID8" with an enhanced assumed strain field is developed to study the global and local buckling behaviors of laminated composite plates with through-the-width or embedded delamination. An efficient three-dimensional finite element model for the delamination has also been presented. The effects of delamination on the buckling loads and modes of the laminated composite plates have been studied using various parameters, such as delamination size, aspect ratio, width-to-thickness ratio, stacking sequences, and location of delamination and multiple delaminations. We find the following key observations in designing composite structures containing delaminations.

1. The buckling characteristics of laminated composite plates analyzed using two- and three-dimensional models are significantly different from each other under different boundary conditions. This is particularly true for large delamination sizes. The performance of the EAS element is largely improved than that of the incompatible element. Therefore, it is desirable to use EAS solid elements for better accuracy.
2. The buckling loads of the clamped [0//90/90/0] laminated plate for $D/a = 0.8$ approach a constant value as the aspect ratio increases. On the other hand, the buckling load for small delamination sizes tends to decrease sharply in the same range. For the simply supported boundaries, the buckling loads for

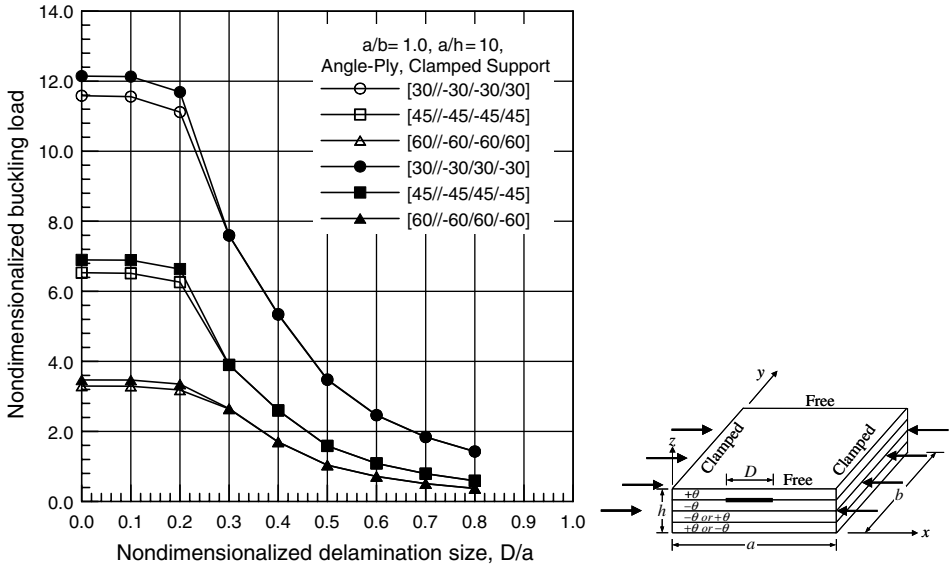

Fig. 14. Nondimensionalized buckling loads versus various through-the-width delamination sizes of clamped symmetric and antisymmetric angle-ply laminated square plates; $a/b = 1.0$, $a/h = 10$.

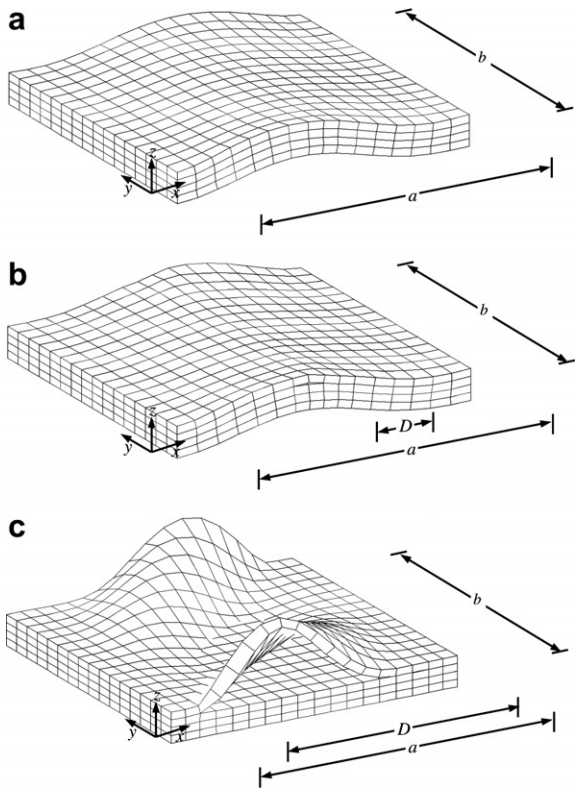

Fig. 15. Buckling modes for whole model of clamped symmetric angle-ply [30//-30/-30/30] laminated square plate with through-the-width single delamination; $a/b = 1.0$, $a/h = 10$. (a) $D/a = 0.0$ (global buckling mode). (b) $D/a = 0.2$ (mixed buckling mode). (c) $D/a = 0.8$ (local buckling mode).

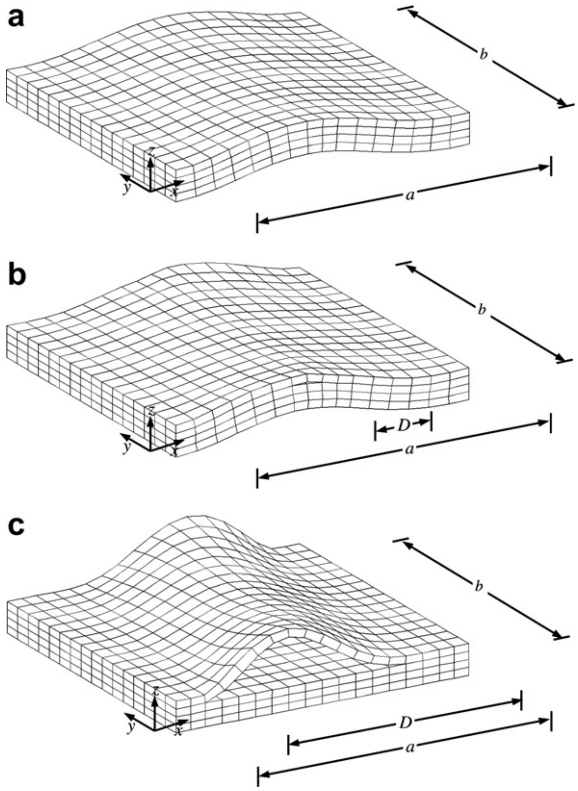

Fig. 16. Buckling modes for whole model of clamped symmetric angle-ply [60//-60/-60/60] laminated square plate with through-the-width single delamination; $a/b = 1.0$, $a/h = 10$. (a) $D/a = 0.0$ (global buckling mode). (b) $D/a = 0.2$ (mixed buckling mode). (c) $D/a = 0.8$ (local buckling mode).

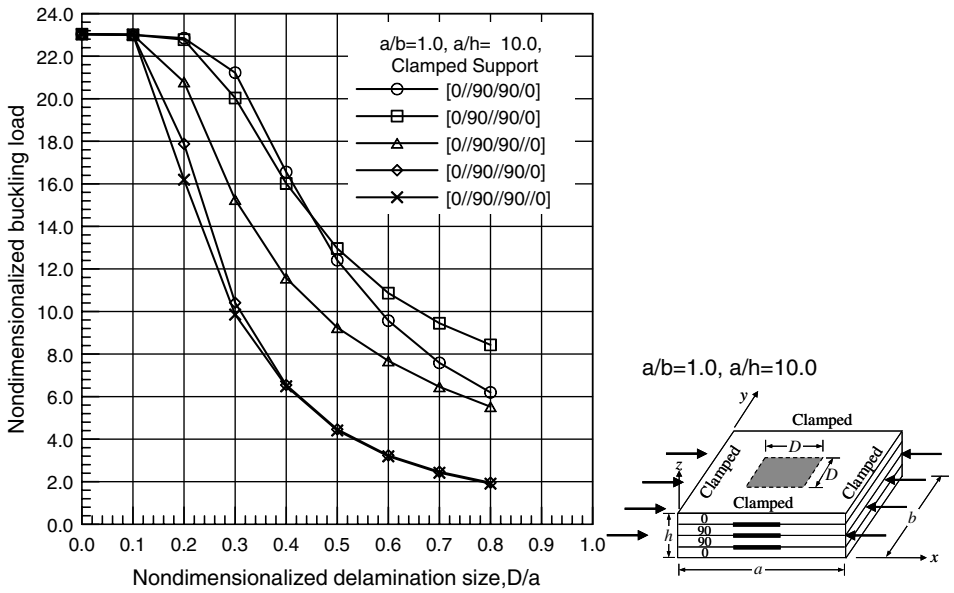

Fig. 17. Nondimensionalized buckling loads versus various delamination sizes of clamped [0/90/90/0] laminated plates with square embedded single delamination or multiple delaminations.

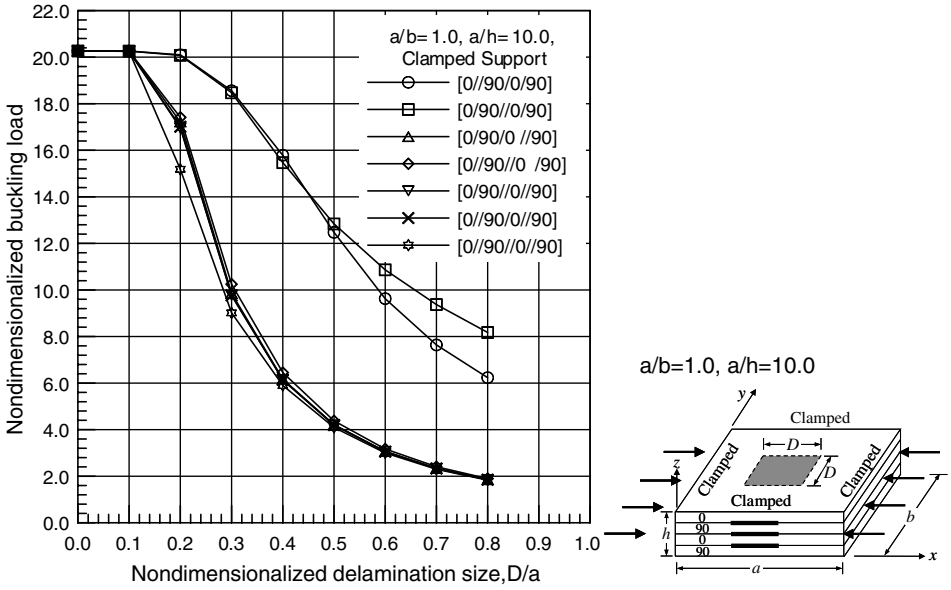

Fig. 18. Nondimensionalized buckling loads versus various delamination sizes of clamped [0/90/0/90] laminated plates with square embedded single delamination or multiple delaminations.

$D/a = 0.0$ and 0.4 are close to each other. On the other hand, the induced buckling load for the delamination size of $D/a = 0.8$ is much lower than those for the other sizes, because the flexural rigidity of the plate should decrease as the delamination size increases. It should be noted that the difference becomes more evident in the case of the clamped plate.

3. For extremely large delamination sizes, the buckling loads approach a constant value regardless of the width-to-thickness ratios; this is because the extremely large delamination size decreases the plate resistance against the local buckling behavior. It is desirable to use the range of $D/a < 0.2$ for a reasonably stable design, particularly for thin composite plates.
4. The induced buckling loads of angle-ply laminates are significantly different for different fiber angles, because different fiber angles largely govern the changes in the bending and shear stiffnesses. The buckling load of the [30//-30/30/-30] laminate exhibits the highest value of the lay-ups considered. The change in the stiffnesses due to the layup sequence is negligible; therefore, the buckling load does not change significantly.
5. The differences in the buckling loads due to the location and number of delaminations show different trends when compared with the symmetric case. This is due to the effect of B_{ij}, which became nonzero for antisymmetric laminates, inducing complicated influences on the buckling behavior of the structural system.

From this study, it may be concluded that the local buckling effects at the laminate face for different geometrical properties should not be neglected and thus three-dimensional models using EAS solid elements should be used to analyze laminated composite structures containing small delaminations for obtaining better accuracy.

References

Andelfinger, U., Ramm, E., 1993. EAS-elements for two-dimensional, three-dimensional, plate and shell structures and their equivalence to HR-elements. Int. J. Numer. Methods Eng. 36, 1311–1337.

Bathe, K.J., 1996. Finite Element Procedures in Engineering Analysis. Prentice-Hall, Englewood Cliffs, NJ.

Bottega, W.J., Maewal, A., 1983. Delamination buckling and growth in laminates. ASME J. Appl. Mech. 50, 184–189.

Braes, D., 1998. Enhanced assumed strain elements and locking in membrane problems. Comp. Methods Appl. Mech. Eng. 165, 155–174.

Chai, H., Babcock, C.A., Knauss, W.G., 1981. One dimensional modeling of failure in laminated plates by delamination buckling. Int. J. Solids Struct. 17, 1069–1083.

Chen, H.P., 1991. Shear deformation theory for compressive delamination buckling and growth. AIAA J. 29, 813–819.
Cheng, Z.Q., Kennedy, D., Williams, F.W., 1996. Effect of interfacial imperfection on buckling and bending behavior of composite laminates. AIAA J. 34, 2590–2595.
Cheung, Y.K., Chen, W., 1988. Isoparametric hybrid hexahedral elements for three dimensional stress analysis. Int. J. Numer. Methods Eng. 26, 677–693.
Gu, H., Chattopadhyay, A., 1999. An experimental investigation of delamination buckling and postbuckling of composite laminates. Compos. Sci. Technol. 59, 903–910.
Hu, N., 1999. Buckling analysis of delaminated laminates with consideration of contact in buckling mode. Int. J. Numer. Methods Eng. 44, 1457–1479.
Jane, K.C., Yin, W.L., 1992. Refined buckling and postbuckling analysis of two-dimensional delaminations-II. Results for anisotropic laminates and conclusion. Int. J. Solids Struct. 29, 611–639.
Kant, T., Manjunatha, B.S., 1988. An unsymmetric FRC laminte C^0 finite element model with 12 degrees of freedom per node. Eng. Comput. 5, 300–308.
Kardomateas, G.A., Schmueser, D.W., 1988. Buckling and postbuckling of delaminated composites under compressive loads including transverse shear effects. AIAA J. 26 (3), 337–343.
Kim, H.J., 1997. Postbuckling analysis of composite laminates with a delamination. Comput. Struct. 62 (6), 975–983.
Kim, J.S., Cho, M., 2002. Buckling analysis for delaminated composites using plate bending elements based on higher-order zig-zag theory. Int. J. Numer. Methods Eng. 55, 1323–1343.
Macneal, R.H., 1987. A theorem regarding the locking of tapered four-noded membrane elements. Int. J. Numer. Methods Eng. 24, 1793–1799.
Noor, A.K., 1975. Stability of multilayered composite plates. Fibre Sci. Technol. 8, 81–88.
Pandya, B.N., Kant, T., 1988. Finite element stress analysis of laminated composite plates using higher order displacement model. Compos. Sci. Technol. 32, 137–155.
Pian, T.H.H., 1982. On the equivalence of non-conforming element and hybrid stress element. Appl. Math. Mech. Engl. Ed. 3 (6), 773–776.
Pian, T.H.H., Sumihara, K., 1984. Rational approach for assumed stress finite elements, Int. J. Numer. Methods Eng. 20, 1685–1695.
Reddy, J.N., 1984. A simple higher order theory for laminated composite plates. ASME J. Appl. Mech. 51, 745–752.
Senthilnathan, N.R., Lim, K.H., Lee, K.H., Chow, S.T., 1987. Buckling of shear deformable plates. AIAA J. 25, 1268–1271.
Sheinman, I., Soffer, M., 1990. Effect of delamination on the nonlinear behavior of composite laminated beams. ASME J. Eng. Mater. Technol. 11, 393–397.
Simitses, G.J., Sallam, S., Yin, W.L., 1985. Effect of delamination of axially loaded homogeneous laminated plates. AIAA J. 23, 1437–1444.
Simo, J.C., Rifai, M.S., 1990. A class of mixed assumed strain methods and the method of incompatible modes. Int. J. Numer. Methods Eng. 29, 1595–1638.
Suemasu, H., Kumagai, T., Gozu, K., 1998. Compressive behavior of multiply delaminated composite laminates Part 1: experiment and analytical development. AIAA J. 36, 1279–1285.
Wang, J.T., Pu, H.N., Lin, C.C., 1997. Buckling of beam-plates having multiple delaminations. J. Compos. Mater. 31, 1002–1025.
Whitcomb, J.D., 1989. Predicted and observed effects of stacking sequence and delamination size on instability related delamination growth. J. Compos. Technol. Res. 11, 94–98.
Whitney, J.M., Pagano, N.J., 1970. Shear deformation in heterogeneous anisotropic plates. ASME J. Appl. Mech. 37, 1031–1036.
Wilson, E.L., Ibrahimbegovic, A., 1990. Use of incompatible displacement modes for the calculation of element stiffnesses or stresses. Finite Elem. Anal. Des. 7, 229–241.
Wu, C.C., Huang, M.G., Pian, T.H.H., 1987. Consistency condition and convergence criteria of incompatible elements: general formulation of incompatible functions and its application. Comput. Struct. 27, 639–644.